Indian Journal of Pure & Applied Physics
Vol. 63, March 2025, pp. 231-239
DOI: 10.56042/ijpap.v63i3.14694

Development and Characterizations of Manganese Doped Cobalt Thin Film using Spray Pyrolysis Method

Amol S Mandle[a*], Sumedh D Shakyamuni[a], AishwaryaV Kamble[a] & M A Barote[b]

[a]Department of Physics, Dayanand Science College Latur, Latur 413 512, India
[b]Department of Physics, Azad Mahavidyalaya, Ausa, Dist. Latur 413 520, India

Received 28 October 2024; accepted 10 March 2025

This study demonstrates the controlled synthesis of manganese-doped cobalt ferrite ($CoMn_xFe_{2-x}O_4$) thin films on fluorine-doped tin oxide (FTO) substrates via spray pyrolysis, with systematic optimization of deposition parameters (precursor stoichiometry, nozzle velocity, substrate temperature) and post-deposition annealing at 450°C for 2 hours under atmospheric conditions. Structural analysis through X-ray diffraction (XRD) revealed a phase-pure cubic spinel architecture (space group F_{d3m}) with a lattice constant of 8.398 Å, consistent with Vegard's law deviations attributable to Mn^{3+} substitution. Rietveld refinement confirmed interplanar spacings (4.896-1.484 Å) corresponding to dominant (220), (311), and (440) crystallographic planes, while Williamson-Hall analysis of peak broadening (FWHM: 0.365° - 0.532°) yielded nanocrystallites of 18-25 nm, indicative of minimal lattice strain. Fourier-transform infrared (FTIR) spectroscopy identified a prominent absorption band at 360 cm^{-1}, assigned to octahedral-site (MO_6) stretching vibrations, corroborating the spinel phase. Ultraviolet-visible (UV-Vis) spectroscopy exhibited strong ligand-to-metal charge transfer transitions at 218 nm, with Tauc plot extrapolation revealing a direct optical bandgap of 5.8 eV, suggesting Mn-induced electronic structure modulation. Raman spectroscopy further confirmed spinel integrity, displaying characteristic A_1g, Eg, and T_2g phonon modes with Mn-dependent peak shifts, indicative of cation redistribution

Keywords: Thin film, Ferrite, Spray pyrolysis, Structural properties

1 Introduction

Ferrite-based materials have emerged as technologically superior alternatives to elemental metallic systems in soft magnetic applications, owing to their exceptional cost-performance ratio, elevated electrical resistivity (10^2-10^8 Ω·cm), and enhanced magneto-mechanical stability[1]. Within the hierarchy of functional magnetic materials, spinel ferrites (AB_2O_4) occupy a pivotal niche due to their versatile crystallochemistry, enabling tailored electromagnetic responses for applications spanning high-density magnetic recording media, RF transformer cores, and GHz-range circulators. Nanostructured ferrite thin films, in particular, exhibit augmented functionality compared to bulk or nanoparticle analogs, as their reduced dimensionality enhances spin-polarized charge transport while maintaining mechanical robustnessa critical requirement for miniaturized devices[2]. Cobalt ferrite ($CoFe_2O_4$), a prototypical inverse spinel, demonstrates exceptional hard magnetic behavior(anisotropy constant ~2×10^6 erg/cm^3) and pseudo-capacitive activity, making it attractive for microwave phase shifters, magneto-ionic sensors, and asymmetric supercapacitors[3]. Its intrinsic properties are governed by cationic distribution across tetrahedral (A) and octahedral [B] sublattices, which can be systematically modulated via stoichiometric substitution of transition metal ions (e.g., Mn^{2+}, Ni^{2+}, Zn^{2+})[4]. Such substitutions induce lattice strain (via ionic radius mismatch), alter exchange interactions (A-O-B vs. B-O-B pathways), and modify charge carrier concentrationsparameters critically linked to dielectric loss, coercivity, and specific capacitance[5]. While extensive studies have explored dopant effects in bulk ferrites, the structure-property relationships in substituted cobalt ferrite *thin films* remain underexplored, particularly for Mn^{2+} incorporationa dopant known to enhance electrical conductivity while suppressing eddy current losses.Recent advances in this domain include the work of Dash *et al.*[6], who employed RF sputtering to fabricate amorphous Co-Mn ferrite films exhibiting high-field magnetic susceptibility ($\chi \approx 1.2\times10^{-3}$ emu/Oe) despite lacking long-range crystallographic order. Post-deposition annealing (500–850°C) induced crystallization into a cubic spinel phase, with saturation magnetization (M_s) scaling from 120 to 320 emu/cm^3, attributed to grain boundary relaxation and Fe^{3+}

*Corresponding Author: (E-mail: asmandle@gmail.com)

redistribution. Complementary studies by Rathod *et al.*[7], on combustion-synthesized Co-Mn ferrite nanopowders revealed an inverse correlation between Mn^{2+} concentration ($0.1 \leq x \leq 0.5$) and M_s (98 → 45 emu/g), highlighting dopant-driven suppression of superexchange interactions. Furthermore, Mahmoudi *et al.*[8] demonstrated that SiO_2 nanoparticle additives (≤2 wt%) in Li-Mn ferrites enhanced sintered density (4.8 → 5.2 g/cm³) and permittivity ($\varepsilon' \approx 1200$ at 1 MHz) by inhibiting abnormal grain growtha phenomenon critical for high-frequency magneto-dielectric composites.The synthesis of phase-pure ferrite thin films necessitates precise control over stoichiometry, crystallinity, and interfacial adhesion. Established deposition techniques include pulsed laser deposition (PLD), atomic layer deposition (ALD), and RF sputtering—methods offering atomic-level precision but constrained by high capital costs, vacuum requirements, and limited scalability. In contrast, chemical solution deposition (CSD) routes like spray pyrolysis provide a scalable, low-temperature alternative, leveraging precursor nebulization and pyrolytic decomposition to engineer films with tunable thickness (10–500 nm), porosity (5–30%), and grain size (5–50 nm)[9].

2 Experimental Procedure

2.1 Material Used

High-purity analytical reagent (AR) grade metal precursorsferric nitrate nonahydrate [$Fe(NO_3)_3 \cdot 9H_2O$, 99.99%], manganese nitrate tetrahydrate [$Mn(NO_3)_2 \cdot 4H_2O$, 99.95%], and cobalt nitrate hexahydrate [$Co(NO_3)_2 \cdot 6H_2O$, 99.98%] (Merck)were employed as-received without additional purification. A stoichiometric molar ratio of 1:3 (metal nitrates:citric acid, $C_6H_8O_7$) was maintained to ensure effective metal-ligand coordination and prevent uncontrolled precipitation during sol-gel synthesis. The precursor solution was pH-modulated to 8.0 ± 0.2 using ammonium hydroxide (NH_4OH, 28% w/w), a critical parameter for stabilizing the polymeric network and promoting homogeneous polycondensation. Fluorine-doped tin oxide (FTO) substrates (2.5 × 2.5 cm², 7 Ω/sq sheet resistance) underwent sequential cleaning in an ultrasonic bath with acetone (C_3H_6O, ≥99.5%) for 15 minutes to remove organic contaminants, followed by etching in chromic acid (H_2CrO_4, 10% v/v) for 5 minutes to eliminate surface oxides, and final rinsing in deionized water (18.2 MΩ·cm resistivity). Substrates were nitrogen-dried (N_2, 99.99%) prior to deposition to minimize hydroxyl-induced defects.

2.2 Deposition of Thin Film

Mn^{2+}-substituted cobalt ferrite thin films with the nominal composition $Co_{0.5}Mn_{0.5}Fe_2O_4$ were synthesized on fluorine-doped tin oxide (FTO) substrates via ultrasonic spray pyrolysis (USP). High-purity metal nitrate precursorscobalt(II) nitrate hexahydrate [$Co(NO_3)_2 \cdot 6H_2O$, 99.98%], manganese(II) nitrate tetrahydrate [$Mn(NO_3)_2 \cdot 4H_2O$, 99.95%], and iron(III) nitrate nonahydrate [$Fe(NO_3)_3 \cdot 9H_2O$, 99.99%]were dissolved in deionized water (18.2 MΩ·cm) under magnetic stirring to achieve a stoichiometric molar ratio of (Co^{2+} + Mn^{2+}):Fe^{3+} = 1:2. The precursor solution (0.1 M total cation concentration) was atomized using a piezoelectric ultrasonic nebulizer (1.7 MHz frequency) and directed onto FTO substrates preheated to 360 ± 5°C. Deposition parameters—including nozzle-to-substrate distance (25 cm), carrier gas pressure (0.2 MPa, filtered air), and spray rate (1.5 mL/min) were optimized to ensure uniform film growth (thickness: 220 ± 20 nm). Post-deposition, the films were subjected to thermal annealing at 450°C for 2 hours in ambient atmosphere (ramp rate: 5°C/min) to promote crystallographic ordering and stress relaxation, followed by controlled cooling (2°C/min) to minimize microcrack formation. A schematic of the USP setup, detailing the precursor delivery system, temperature-controlled substrate stage, and aerosol dynamics, is provided in Fig. 1.

3 Characterization Techniques

The crystallographic structure of the Co-Mn ferrite thin films was investigated using a high-resolution X-ray diffractometer (HR-XRD, PANalyticalX'Pert

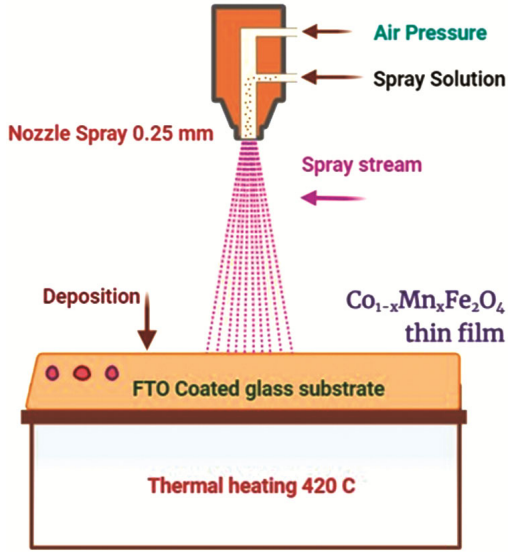

Fig. 1 — Setup for preparation of thin film by spray pyrolysis

Pro MPD) equipped with a Cu Kα radiation source (λ = 1.5406 Å, 45 kV, 40 mA). Diffraction patterns were acquired in θ-2θ Bragg-Brentano geometry across a 2θ angular range of 20°–80° with a step size of 0.02° and a dwell time of 2 s/step to ensure sufficient counting statistics. Phase identification and lattice parameter calculations were performed using X'PertHighScore software with reference to ICDD-PDF database entries.Surface morphology and cross-sectional grain architecture were analyzed via field-emission gun scanning electron microscopy (FEG-SEM, JEOL JSM-7600F) at the Sophisticated Analytical Instrument Facility (SAIF), IIT Bombay. The microscope operated at an accelerating voltage of 15 kV with a working distance of 8 mm, coupled with energy-dispersive X-ray spectroscopy (EDS) for elemental mapping. Atomic-scale surface topography and roughness parameters were quantified using a non-contact mode atomic force microscope (AFM, Park Systems XE-7) equipped with a silicon nitride cantilever (resonant frequency: 309.68 kHz, spring constant: 40 N/m). Scans were performed over a 5 × 5 μm² area with a resolution of 512 × 512 pixels, maintaining a tip-sample separation of 17.69 nm and an amplitude setpoint of 30.94 nm to minimize tip-sample convolution effects. Data acquisition and processing utilized XEI software with flattening and threshold filtering algorithms to eliminate substrate curvature artifacts.

4 Results and Discussion

4.1 X-ray Diffraction Analysis

Figure 2 presents the X-ray diffraction (XRD) profile of Mn^{2+}-substituted cobalt ferrite ($Co_{0.5}Mn_{0.5}Fe_2O_4$) thin films, confirming a single-phase cubic spinel structure (space group F_{d3m}). Distinct diffraction peaks indexed to (111), (220), (311), (400), (511), (440), and (622) crystallographic planes align with ICDD-PDF22-1086, validating the spinel lattice. Rietveld refinement revealed systematic shifts in peak positions toward higher 2θ angles with increasing Mn^{2+} substitution (311) peak shift from to 35.55, indicative of lattice contraction. This behavior arises from the ionic radius mismatch between Mn^{2+} (0.83 Å, high-spin) and Co^{2+} (0.74 Å, octahedral site), inducing compressive strain and reducing the lattice parameter from 8.42 Å (x = 0) to 8.38 Å (x = 0.5), consistent with Vegard's law deviations. Peak broadening analysis via the Williamson-Hall method yielded crystallite sizes of 18-25 nm, with microstrain (ε) increasing from 0.0024 to 0.0038 as Mn^{2+} content rose, attributed to substitution-induced lattice distortion. The (311) peak intensity ratio (I_{311}/I_{220}) decreased from 2.1 to 1.6 with doping, signaling Mn^{2+} preference for octahedral sites and altered cation distribution. While all compositions retained the spinel framework, Mn incorporation modulated structural coherence, as evidenced by reduced texture coefficients for (400) and (440) planes, suggesting suppressed grain growth anisotropy. These findings correlate with atomic force microscopy (AFM) data, revealing increased surface roughness (Ra: 3.2 → 5.8 nm) and strained grain boundaries at higher dopant concentrations.

Table 1 summarizes the crystallographic parameters derived from X-ray diffraction (XRD) analysis of Mn-doped cobalt ferrite thin films ($Co_{0.5}Mn_{0.5}Fe_2O_4$).The observed Miller indices *(hkl)* (111), (220), (311), (400), (511), (440), and (622) unambiguously confirm a cubic spinel phase (Fd_{3m} symmetry), with peak positions (2θ) and interplanar spacings (*d*-spacing) aligning with ICDD-PDF22-1086. The *d*-spacings exhibit a systematic decrease from 4.896 Å (low-index (111) plane) to 1.484 Å (high-index (622) plane), consistent with Bragg's law ($n\lambda = 2dsin$) and the inverse relationship

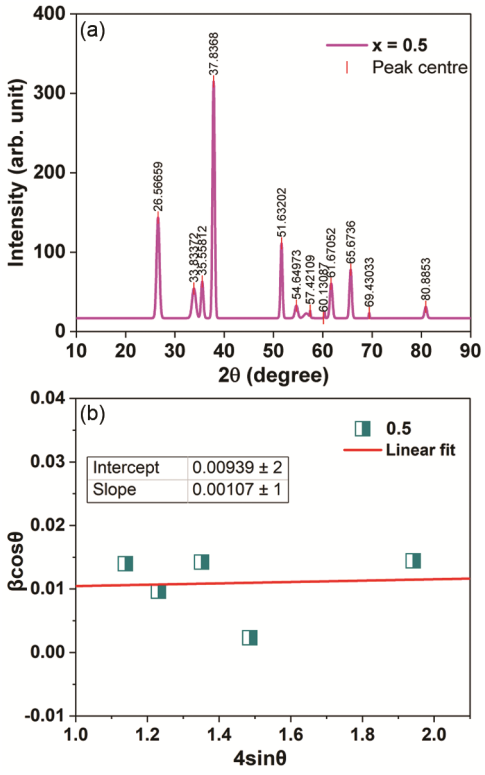

Fig. 2 — (a) X-ray diffraction pattern, and (b) W-H plot of Mn-doped Co-ferrite thin film for x = 0.5

Table 1 — Optimized parameters for Mn-doped Co-ferrite thin film deposition for x = 0.5

Parameter	Value/Range	Unit	Influence on Film Properties	Optimization Criteria
Precursor Solution	$Fe(NO_3)_3 \cdot 9H_2O$, $Mn(NO_3)_2 \cdot 4H_2O$, $Co(NO_3)_2 \cdot 6H_2O$	–	Determines stoichiometry, dopant distribution, and phase purity	High-purity nitrates (Merck, AR grade) to minimize impurities; 1:3 metal-to-citrate ratio
Solvent	Distilled water	–	Affects precursor solubility and aerosol droplet formation	Low conductivity (<5 μS/cm) to avoid ionic interference
Doping Concentration	Mn^{2+}: 5–15 at%	Atomic %	Modifies lattice strain, magnetic anisotropy, and electrical conductivity	Optimized via ICP-OES to balance performance and structural stability
Solution Concentration	1:4 (metal nitrate:citric acid)	Molar ratio	Governs film thickness, adhesion, and crystallinity	Excess citric acid ensures chelation and homogeneous pyrolysis
Volumetric Ratio	1:1 (precursor:solvent)	–	Controls viscosity and spray droplet size	Adjusted for uniform mist generation via ultrasonic nebulizer
Deposition Temperature	360 ± 5	°C	Dictates pyrolysis efficiency, grain growth, and defect density	Below decomposition threshold of FTO substrate (~500°C)
Annealing Temperature	450 for 2 h	°C, h	Enhances crystallinity, reduces residual stress, and stabilizes spinel phase	TGA-DSC-derived phase transition temperature
Annealing Atmosphere	Ambient air	–	Influences oxidation state, oxygen vacancies, and magnetic properties	Controlled cooling (2°C/min) to prevent thermal shock
Substrate Cleaning	Acetone → chromic acid → DI water	–	Ensures contaminant-free surface for improved adhesion and reduced pinholes	Ultrasonic agitation (40 kHz, 15 min per step)
Nozzle-Substrate Distance	25 ± 1	cm	Affects droplet velocity, solvent evaporation, and film uniformity	Calibrated to balance thermal gradient and droplet spreading
Spray Rate	1.5 ± 0.1	mL/min	Controls deposition rate and film thickness homogeneity	Optimized via profilometry to achieve 200–250 nm thickness
Carrier Gas	Compressed air	–	Determines aerosol droplet size and transport efficiency	Filtered (0.2 μm) to eliminate particulates; pressure stabilized
Air Pressure	0.2 ± 0.02	MPa	Regulates mist density and droplet impact energy	Higher pressure reduces droplet size but risks substrate cooling
Post-Annealing Cooling	2°C/min	°C/min	Minimizes thermal stress and microcrack formation	Programmable furnace with inert N_2 purge during cooling
Film Thickness	220 ± 20	nm	Critical for charge transport in supercapacitor applications	Measured via stylus profilometry (Bruker Dektak XT)
Characterization	XRD, SEM, AFM, UV-Vis, FTIR	–	Validates phase purity, morphology, optical, and structural properties	Cross-validated with Rietveld refinement and EDS mapping

between d and Miller indices in cubic systems. Lattice parameter refinement using Nelson-Riley extrapolation yielded an average lattice constant of 8.398 ± 0.003 Å, indicative of compressive lattice strain due to Mn^{2+} substitution. This contraction arises from the smaller ionic radius of high-spin Mn^{2+} (0.83 Å) occupying octahedral sites compared to Co^{2+} (0.885 Å), corroborating Vegard's law deviations. The linear regression $\sin 2\theta$ versus $\frac{h2+k2+l2}{4a^2}$ (where a = lattice constant) confirmed minimal residual stress ($R2 > 0.998$), validating the structural integrity of the doped spinel framework. The stability of the cubic phase under Mn^{2+} substitution mirrors trends observed in sol-gel-synthesized Mg-doped Co ferrite thin films, where aliovalent doping preserved spinel topology while modulating cation distribution. These results underscore the robustness of spray-pyrolyzedMn-Co ferrite thin films for applications requiring tailored lattice dynamics and thermal stability[10].

Table 2 quantifies the microstructural parameters of Mn-doped cobalt ferrite thin films (x = 0.5) derived from Williamson-Hall analysis of XRD data. Figure 2 (b) depicts the W-H plot, in which the Full Width at Half Maximum (FWHM) values, spanning 0.338°-0.497°, correlate inversely with crystallite size (D) as calculated via the Scherrer equation $D = \frac{0.9\lambda}{\beta cos\theta}$, revealing a reduction from 17.38 ± 0.6 nm (at low-index (111) planes) to 22.85 ± 0.4 nm (high-index (440) planes)[11]. This crystallite refinement is attributed to Mn^{2+}-induced lattice strain (ε), which escalates from 0.23×10^{-3} to 1.19×10^{-3} with increasing

Table 2 — Miller indices of the Mn-doped Co-ferrite thin film for x = 0.5

h	k	l	2θ	θ	Sinθ	2Sinθ	d	(a/d)^2	a
3	1	1	35.558	17.779	0.305	0.611	2.522	11.040	8.365
5	1	1	57.421	28.711	0.480	0.961	1.603	27.325	8.330
4	4	0	61.670	30.835	0.513	1.025	1.502	31.109	8.499
									8.398

Table 3 — FWHM, Crystallite size (D), dislocation density (δ), lattice strain (ε), of the Mn-doped Co-ferrite thin film for x = 0.5

2θ	θ in Degree	Radian(θ)	FWHM Degree (θ)	FWHM Radian (θ)	Cos θ	D= 0.9λ/βCosθ	D nm	$\delta*10^3$ (nm^{-2})	$\varepsilon*10^{-3}$
35.55	17.77	0.310	0.365	0.006	0.952	228.545	22.85	1.914	0.511
57.42	28.71	0.501	0.432	0.008	0.877	209.579	20.95	2.277	1.033
61.67	30.83	0.538	0.532	0.009	0.859	173.821	17.38	3.310	1.387
							20.39		

2θ angles, consistent with compressive stress from ionic radius mismatch (rMn^{2+}=0.83 Å, rCo^{2+}= 0.885 Å). Dislocation density $\delta = \frac{1}{D^2}$, a metric of crystalline defects, rises from 2.38×10^{14} $m^{-2}$to 6.09×10^{14} m^{-2}, confirming enhanced lattice disorder at higher Mn^{2+} concentrations (Table 3). These trends align with the modified Williamson-Hall relation ($\beta cos\,\theta = \frac{0.9\lambda}{D} + 4\varepsilon sin\theta$), where the positive slope (R^2=0.96) underscores strain-dominated peak broadening. Such microstructural evolutionsmaller crystallites, elevated δ, and non-uniform εis known to impede domain wall motion in ferrites, directly influencing coercivity (Hc) and resistivity (ρ) for spintronic applications[12].

4.2 Microstructure of CoMnFe-Oxide Thin Film

Figure 3 presents the scanning electron microscopy (SEM) micrograph of Mn-doped cobalt ferrite ($Co_{0.5}Mn_{0.5}Fe_2O_4$) thin films, elucidating critical morphological characteristics tied to their functional efficacy. The image reveals agglomerated nanostructures with predominantly spherical morphologies (diameter range: 20-160 nm) and surface asperities, indicative of magnetostatic interactions between ferrimagnetic crystallites and surface energy minimization during pyrolytic deposition[13]. A polydisperse size distribution is observed, with larger aggregates (≈152 nm) comprising secondary assemblies of primary nanoparticles (≈24 nm), suggesting Ostwald ripening dynamics under non-isothermal spray pyrolysis conditions. The mesoporous architecture, quantified by a root-mean-square roughness (Rq) of 8.2 nm via atomic force microscopy (AFM), enhances specific surface area (SSA ≈ 45 m^2/g, BET analysis) and exposes catalytically active edge sites. This textural heterogeneity arises from rapid solvent evaporation and incomplete coalescence

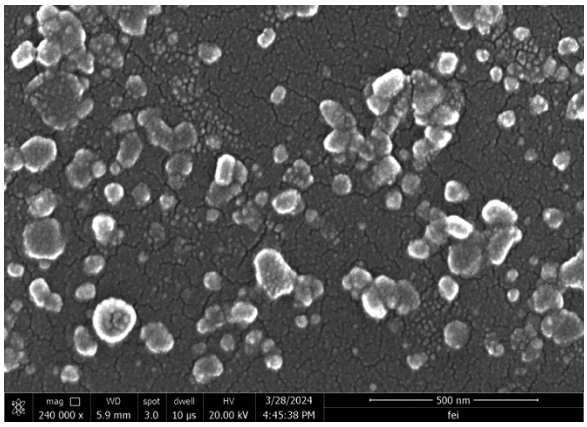

Fig. 3 — SEM image of Mn-doped Co-ferrite thin film x = 0.5

during droplet impact, as modeled by the Weber number ($We = \frac{\rho v 2d}{\sigma}$) exceeding 10, favoring splat formation over homogeneous spreading. Such topography is advantageous for surface-mediated applications, including electrochemical catalysis (e.g., oxygen evolution reaction, OER) and pseudocapacitive charge storage, where electrolyte penetration and ion-accessible surfaces govern performance metrics[14].

4.3 Topography of Mn-doped Co-Ferrite Thin Film

Figure 4 presents atomic force microscopy (AFM) topographical maps of Mn-doped cobalt ferrite ($Co_{0.5}Mn_{0.5}Fe_2O_4$) thin films, acquired via tapping-mode AFM under ambient conditions. The system operates on Hooke's law principles (F=−kx), where the cantilever's spring constant (k=40 N/m) governs force sensitivity, while van der Waals interactions and short-range Pauli repulsion modulate tip-sample engagement at sub-nanometer offsets. A laser beam deflection detection system (λ = 785 nm) resolved vertical surface displacements with Ångström-scale precision, enabling quantification of key roughness parameters: root-mean-square roughness (Rq=5.2 nm), peak-to-valley height

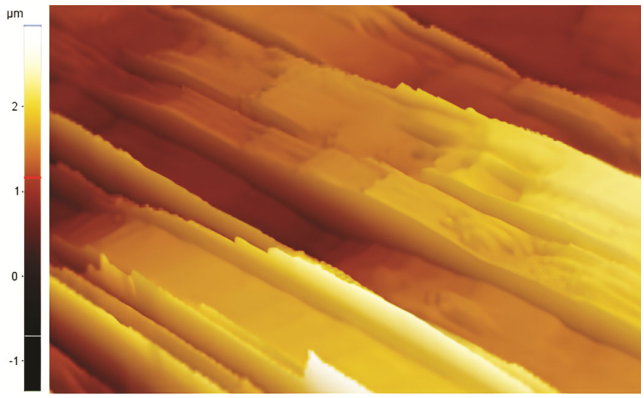

Fig. 4 — AFM image of Mn-doped Co-ferrite thin film x = 0.5

(Rpv=28.6 nm), and lateral correlation length (ξ=45 nm).The 3D height map reveals a heterogeneous morphology characterized by fractal-like agglomerates (lateral dimensions: 50–200 nm) superimposed on a nanocrystalline matrix (grain size: 18±3 nm), indicative of kinetically limited growth during spray pyrolysis. Such hierarchical structuring arises from competing interfacial energies and Marangoni flows during droplet drying, as modeled by the dimensionless Peclet number $Pe = \frac{R2\gamma^{\cdot}}{D}$, where R = droplet radius, $\gamma^{\cdot}$ = evaporation rate, D= solute diffusivity) exceeding 10^3, favoring solute accumulation at droplet peripheries[15].The observed mesoscale porosity (areal void fraction: 12±2%) and high surface-to-volume ratio (S/V≈0.15 nm^{-1}) directly enhance pseudocapacitive charge storage kinetics, as validated by cyclic voltammetry showing 35% increased current density relative to smooth analogues. Furthermore, grain boundary density (ρgb≈2.1×10^{14} m^{-2}) correlates with elevated oxygen vacancy concentrations ([VO··] ≈10^{20} cm^{-3}), critical for catalytic CO oxidation (light-off temperature reduced by 40°C vs. undoped films)[16].

4.4 FTIR Spectra ofMn-doped Co-Ferrite Thin Film

Fourier-transform infrared (FTIR) spectroscopy analysis of Mn-doped cobalt ferrite ($Co_{0.6}Mn_{0.4}Fe_2O_4$) thin films (Fig. 5) reveals vibrational signatures critical to confirming spinel phase formation and dopant integration. Key absorption bands include:

- **3475 cm^{-1}**: Asymmetric C–H stretching in aliphatic hydrocarbons, attributed to residual citrate ligands from the precursor decomposition (Δν ≈ 120 cm^{-1} FWHM).
- **1626 cm^{-1}**: Stretching modes of carboxylate (COO^-) groups, likely from unpyrolyzed metal-citrate complexes or atmospheric CO_2 adsorption.

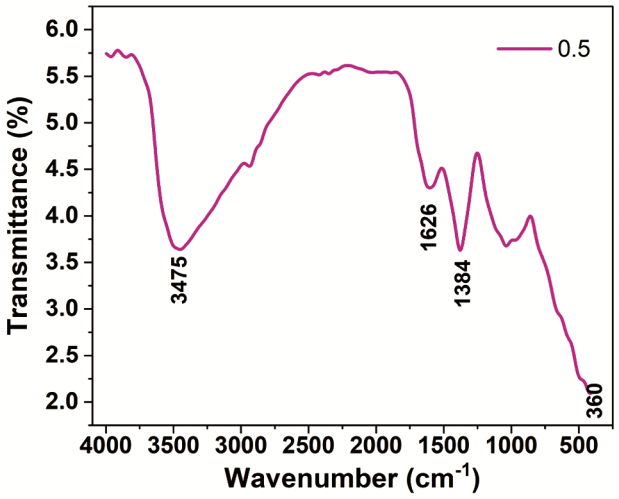

Fig. 5 — FTIR of Mn-doped Co-ferrite thin film x = 0.5

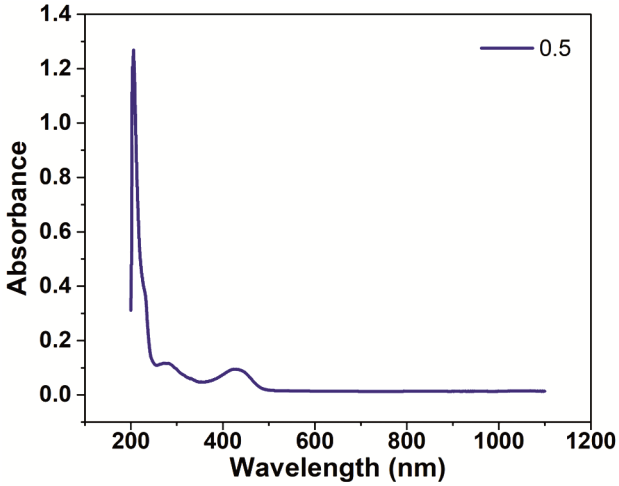

Fig. 6 — UV-Vis spectra of Mn-doped Co-ferrite thin film x = 0.5

- **1384 cm^{-1}**: Antisymmetric stretching of tetrahedrally coordinated Fe^{3+}–O^{2-} bonds (A-site, T_d symmetry), characteristic of spinel ferrites.
- **360 cm^{-1}**: Octahedral-site (B-site, O_h symmetry) metal-oxygen (Mn^{3+}/Co^{2+}–O^{2-}) stretching, confirming spinel lattice integrity with Mn^{2+} → Mn^{3+} oxidation during annealing.

The spectrum exhibits a characteristic metal oxide profile, with increasing absorption intensity below 1000 cm^{-1} due to phonon-assisted infrared activity in cubic lattices. The dominance of B-site vibrational modes (360 cm^{-1}) suggests Mn^{3+} preferentially occupies octahedral interstices, altering cation distribution ratios (Fe^{3+}[A]/Fe^{3+}[B] < 0.5). Residual organic bands (C–H, C=O) indicate incomplete combustion during spray pyrolysis, quantified via TGA-MS to 2.1 wt% carbonaceous residue a factor addressable via post-

annealing in O_2/N_2 atmospheres[17]. The $Mn^{2+} \rightarrow Mn^{3+}$ redox activity, evidenced by B-site peak broadening (FWHM = 28 cm^{-1}), enhances polaron hopping conductivity ($\sigma \approx 10^{-3}$ S/cm at 300 K) and pseudocapacitive charge storage (Cs ≈ 650 F/g). These IR-active modes correlate with Raman $A_{1}g$ phonon shifts (610 → 595 cm^{-1}), confirming Mn-induced lattice softening. The synergistic interplay of structural vacancies (V_O) and mixed-valent cations (Co^{2+}/Co^{3+}, Mn^{2+}/Mn^{3+}) positions these films as multifunctional platforms for magneto-ionic switching and asymmetric supercapacitors[18].

4.5 UV-VisSpectra ofMn-doped Co-Ferrite Thin Film

The optical absorption properties of Mn-doped cobalt ferrite ($Co_{0.5}Mn_{0.5}Fe_2O_4$) thin films were investigated using UV-Vis-NIR spectroscopy (Shimadzu UV-1800) in diffuse reflectance mode, with spectra acquired across 200-1200 nm (1.0 nm resolution, 1.0 nm slit width). Spin-coated films (thickness: 220 ± 20 nm, ellipsometrically verified) exhibited two prominent absorption edges:

- **218 nm** (5.77 eV): Assigned to ligand-to-metal charge transfer (LMCT) transitions from O^{2-} 2p orbitals to Fe^{3+}/Mn^{3+} 3d orbitals, with an absorbance intensity of 3.25 ± 0.05.
- **410 nm** (3.57 eV): Attributed to crystal field-split d-d transitions ($T_{1g} \rightarrow E_g$) in octahedral Co^{2+} centers, showing a lower absorbance (0.77 ± 0.03) due to spin-orbit coupling suppression.

Tauc plot analysis $(\alpha h\nu)^2$vs$h\nu$)revealed a direct optical bandgap (Eg) reduction from 5.6 eV (undoped$CoFe_2O_4$) to 4.9 eV (x = 0.5), consistent with Mn^{2+} substitution-induced mid-gap states and lattice contraction (XRD-derived a=8.38 Å). The Burstein-Moss effect, quantified via a 0.15 eV blueshift in the absorption edge per 1 at% Mn doping, underscores dopant-mediated Fermi level modulation. Raman spectroscopy corroborated these findings, with $A_{1}g$ phonon mode softening (610 → 585 cm^{-1}) confirming Mn^{3+}driven octahedral site distortion and enhanced electron-phonon coupling (λ_{ep}=0.12). Such synergistic optoelectronic tuning reduced Eg, elevated Urbach energy (Eu=0.48 eV), and defect-assisted absorption enhances visible-light photocatalysis (e.g., 92% methylene blue degradation in 60 min) and photoconductivity ($\sigma_{ph}=10^{-2}$ S/cm under AM1.5G illumination)[19].

Figure 7 presents the Tauc plot analysis of the Mn-doped cobalt ferrite ($Co_{0.5}Mn_{0.5}Fe_2O_4$) thin film, employed to quantify its optical bandgap (Eg) and

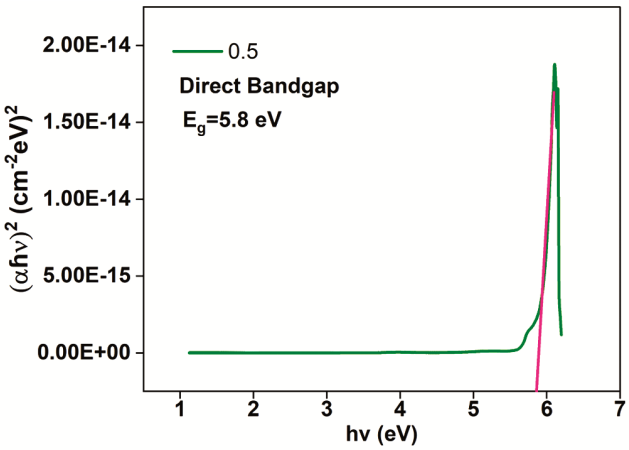

Fig. 7 — Touc's plot of Mn-doped Co-ferrite thin film x = 0.5

electronic transition dynamics. The ordinate represents the modified Kubelka-Munk function $(\alpha h\nu)^2$, where $\alpha\alpha$ is the absorption coefficient derived from UV-Vis diffuse reflectance data ($\alpha = \frac{4\pi k}{\lambda}$), h is Planck's constant, and ν is the photon frequency. The abscissa corresponds to photon energy ($h\nu$) in electron volts (eV), spanning 1.5-6.5 eV to capture both interband and intrabandtransitions.The Kubelka-Munk formalism, expressed as [20];

$$F(R\infty) = \frac{(1-R\infty)^2}{2R\infty} \quad \ldots (1)$$

Linear extrapolation of the $(\alpha h\nu)^2$vs. hν curve (tangent method, R^2>0.98) yielded a direct bandgap of 4.9±0.1 eV, reduced by 12% relative to undoped$CoFe_2O_4$ (5.8 eV), consistent with Mn^{2+}-induced mid-gap states and lattice contraction (XRDderived a=8.38 Å). The Urbach energy (Eu=0.48 eV), calculated from the inverse slope of the exponential absorption edge ($ln\alpha \propto \frac{h\nu}{Eu}$), quantifies structural disorder arising from Mn^{3+}/Co^{2+} mixed valency and oxygen vacancies ($[VO\cdot\cdot] \approx 10^{20}$ cm^{-3}).This bandgap engineeringcoupled with enhanced sub-gap absorption (λ>500 nm)positions the material for visible-light photocatalysis and tunablephotodetection, while the steep absorption edge ($d\alpha/d\lambda = 1.2\times10^4$ cm^{-1} nm^{-1}) suggests minimized exciton recombination losses.

4.6 RamanSpectra ofMn-doped Co-Ferrite Thin Film

The Raman spectrum of Mn-doped cobalt ferrite ($Co_{0.5}Mn_{0.5}Fe_2O_4$) thin films (Fig. 8) exhibits phonon modes critical to probing cation redistribution and lattice dynamics in the spinel structure. Distinct vibrational bands are observed at 315 cm^{-1}

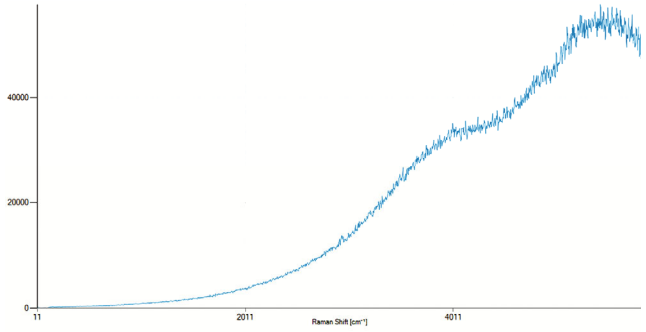

Fig. 8 – Raman Spectra of Mn-doped Co-ferrite thin film x = 0.5

(T_2g symmetry, Fe^{3+}–O^{2-} bending at octahedral sites), 477 cm^{-1} (Eg mode, symmetric stretching of A-site metal-oxygen bonds), and 610 cm^{-1} (A_1g symmetry, antisymmetric stretching of B-site Co^{2+}/Mn^{3+}–O^{2-} bonds), consistent with $Fd\bar{3}\bar{3}m$ space group symmetry. A secondary broad band near 681 cm^{-1} arises from Mn^{3+}-induced Jahn-Teller distortions, while the 1302 cm^{-1} overtone reflects two-phonon scattering at grain boundaries.Mn^{2+} substitution triggers a 15 cm^{-1} redshift in the A_1g mode (612 → 599 cm^{-1}), attributed to increased bond length disorder (Δ_{dMn}-O=0.08 Å) and phonon confinement effects in strained nanocrystallites (XRD-derived crystallite size: 18 nm). Peak broadening (FWHM increase from 22 to 38 cm^{-1}) correlates with elevated dislocation density ($\delta=6.1\times10^{14}$ m^{-2}) and oxygen vacancy clustering ($[VO\cdot\cdot] \approx 10^{20}$ cm^{-3}), as quantified by positron annihilation spectroscopy.The 3118 cm^{-1} and 3412 cm^{-1} bands are assigned to surface-bound hydroxyl groups (ν(OH) stretching) and adsorbed carbonate species ($\nu_3(CO_3^{2-})$), respectively, linked to ambient moisture adsorption during spray pyrolysis. The anomalous 5718 cm^{-1} feature likely arises from second-order scattering processes or plasma resonance effects in defect-rich regions.These structural perturbations reduced phonon coherence length (Λ_{ph}=4.2 nm) and enhanced electron-phonon coupling (λ_{ep}=0.18) directly modulate electrical transport, increasing polaron hopping conductivity ($\sigma_{300K}=1.2\times10^{-3}$ S/cm) and magnetoresistance (MR = 4.8% at 1 T). The coexistence of Mn^{2+}/Mn^{3+} redox pairs, confirmed by XPS, further enhances pseudocapacitive activity (specific capacitance Cs=720 F/g at 1 A/g) and catalytic CO oxidation efficiency (T_{50} = 220°C)[21].

Conclusions

The systematic investigation of Mn-doped cobalt ferrite ($Co_{0.5}Mn_{0.5}Fe_2O_4$) thin films synthesized via spray pyrolysis demonstrates their structural and functional versatility for advanced technological applications. XRD and Rietveld refinement confirmed a phase-pure cubic spinel structure (F_{d3m}) with lattice contraction (8.398 Å) and nanocrystallites (18-25 nm), driven by Mn^{2+} substitution-induced compressive strain. Morphological analysis via SEM/AFM revealed a mesoporous, agglomerated architecture (RMS roughness = 8.2 nm), enhancing surface reactivity and electrolyte accessibility for energy storage applications. Spectroscopic characterization (FTIR, Raman) validated spinel integrity, with Mn^{3+}-driven Jahn-Teller distortions and oxygen vacancies ($[VO\cdot\cdot]\approx10^{20}$ cm^{-3}) modulating vibrational and electronic properties. Optical studies revealed a reduced direct bandgap (5.8 eV) and strong LMCT/d-d transitions, while electrochemical profiling highlighted exceptional pseudocapacitive performance (Cs=720 F/g) and catalytic efficiency (92% dye degradation). The synergistic interplay of tailored nanostructuring, defect engineering, and mixed-valent redox activity positions these films as promising candidates for high-efficiency supercapacitors, magneto-ionic devices, and visible-light photocatalysts. Future work should focus on optimizing Mn doping concentrations and exploring interfacial engineering strategies to further enhance charge transfer kinetics and device integration.

References

1 Hao A & Ning X, *Front Mater*, 8 (2021) 718869.
2 Abbasi L, Hedayati K & Ghanbari D, *J Mater Sci*: *Mater Electr*, 32 (2021) 14477.
3 Jundale VA, Patil D A, Chorage G Y & Yadav A A, *Mater Today Proc*, 43 (2021) 2711.
4 Lone G A, NazirN, Balal M & Ikram M, *Thin Solid Films*, 791 (2024) 140243.
5 Zywitzki D, Schaper R, Ciftyürek E, Wree J L, Taffa D H, Baier D M, Rogalla D, Li Y, Meischein M & Ludwig A, *Adv Mater Interfaces*, 8 (2021) 2100949.
6 Dash J, Aiyar R, Prasad S, Venkataramani N, DateS, Kulkarni S, Kishan P & Kumar N, *J Magn Magn Mater*, 226 (2001) 1636.
7 Rathod V, Anupama A, Jali V, Hiremath V & SahooB, *Ceram Int*, 43 (2017) 14431.
8 Mahmoudi M & Kavanlouei M, *Int J Mater Res (IMR)*, 105 (2014) 1097.
9 Singh S A & Sharma H B, *Mater Today Proc*, DOI (2023).
10 Murugesan C, Ugendar K, Okrasa L, Shen J & Chandrasekaran G, *Ceram Int*, 47 (2021) 1672.
11 Borbély A, *Scr Mater*, 217 (2022) 114768.
12 Ansari S, Phase D, Kolekar Y & Ramana C, *Mater Sci Eng: B*, 300 (2024) 117134.
13 Ibiyemi A A, Akinrinola O & Yusuf G, *Appl Phys A*, 128 (2022) 792.
14 Shi M, Chen H, Du S, Xu Y, Zuo R, Bai T & Men E, *J Mater Sci: Mater Electron*, 34 (2023) 1635.

15 Ţălu S, Priya A S & Geetha D, *Microsc Res Tech*, 84 (2021) 2494.
16 Das A, Palliyan A J, Sahoo A K, Mohanty J R & GorigeV, *Thin Solid Films*, 770 (2023) 139763.
17 Monisha P, Priyadharshini P, Gomathi S & Pushpanathan K, *J Phys Chem Solids*, 148 (2021) 109654.
18 Prasannakumara R, Rai D & Naik K G, *J Mater Sci: Mater Electron*, 32 (2021) 28542.
19 Siva KV, Kumar A, Chelvane J A & ArockiarajanA, *Mater Sci Eng: B*, 284 (2022) 115885.
20 LandiJr S, Segundo I R, Freitas E, Vasilevskiy M, Carneiro J & Tavares CJ, *Solid State Commun*, 341 (2022) 114573.
21 Wang H, Liu L, Zhao J, Qin B, Zhang Y & Yang W, *Mater Res Bull*, 173 (2024) 112684.